Small-Molecule Mimicry Intercepts PEX5 Recognition by Trypanosomal PEX14 as Revealed by Molecular Dynamics

Amanda R. Guimarães[1*], Esther R. S. Paz[1,2], Allison Serrano-Trejos[3], Chonny Herrera-Acevedo[3], Iván Rivilla[4,5], Oscar R. Ballesteros[5], Caroline R. Kwawu[1,6], Guilherme A. M. Jardim[2], Eufrânio N. da Silva Júnior[2], Felipe Fantuzzi[1]

[1]Supramolecular, Interfacial and Synthetic Chemistry, School of Natural Sciences, University of Kent, Park Wood Rd, Canterbury, CT2 7NH, United Kingdom.
[2]Departamento de Química, Instituto de Ciências Exatas, Universidade Federal de Minas Gerais, Belo Horizonte, 31270–901, MG, Brazil.
[3]Department of Chemical Engineering, Universidad ECCI, Bogotá D.C, 111311, Colombia.
[4]Donostia International Physics Center (DIPC), Manuel Lardizabal Ibilbidea, 4, San Sebastián/Donostia, 20018, Gipuzkoa, Spain.
[5]Department of Organic Chemistry I, Center of Innovation in Advanced Chemistry, Faculty of Chemistry (ORFEO CINQA), University of the Basque Country (UPV/EHU), Av. Tolosa, 72, San Sebastián/Donostia, 20018, Gipuzkoa, Spain.
[6]Department of Chemistry, Kwame Nkrumah University of Science and Technology, Kumasi, UPO, AK-385-1973, Ghana.

*Corresponding author(s). E-mail(s): a.ribeiro-guimaraes@kent.ac.uk;
Contributing authors: e.paz-104@kent.ac.uk;
allisonju.serranotr@ecci.edu.co; cherreraa@ecci.edu.co;
ivan.rivilla@ehu.eus; oscar.rodriguez@dipc.org; c.kwawu@kent.ac.uk;
guilhermeamj@ufmg.br; eufranio@ufmg.br; f.fantuzzi@kent.ac.uk;

Abstract

Human trypanosomiases, including Chagas disease and human African trypanosomiasis, remain major neglected tropical diseases with limited therapeutic options and substantial treatment-associated toxicity. In trypanosomatids, glycolytic enzymes are compartmentalised within glycosomes, peroxisome-like organelles whose biogenesis depends on the essential interaction between the peroxins PEX5 and PEX14. Interference with this protein–protein interface therefore represents a promising strategy for developing new trypanocidal agents. Here, molecular docking, MD simulations, and MM–PBSA calculations were used to examine the PEX5–PEX14 interaction and small-molecule binding to the PEX14 recognition groove. The PEX5–PEX14 complex was stabilised by contacts centred on the canonical Wxxx(F/Y) motif of PEX5, particularly Trp60 and Tyr64, with additional contributions from a secondary non-canonical PEX5 region. Hydrogen bonds, salt bridges, π–cation contacts, and T-shaped aromatic interactions involving PEX14 residues Phe12, Phe29, Lys33, and Thr21 were key contributors to complex stability. The reported inhibitor ET7 reproduced central features of the native PEX5 recognition motif and remained associated with the PEX14 groove throughout the simulations. SuFEx-functionalised naphthoquinones from a previously reported series were then assessed as potential PEX14 ligands. While the initial sulfonyl fluoride derivative associated only transiently with the groove, SuFEx derivatisation at the sulfonyl centre to introduce an additional aromatic substituent increased residence time and gave more favourable MM–PBSA binding free energies. These results identify aromatic and electrostatic contacts as major determinants of ligand stabilisation within the PEX14 groove and support SuFEx-derived naphthoquinones as promising scaffolds for inhibitors targeting glycosomal protein import in *Trypanosoma* species.

Keywords: PEX5–PEX14, Protein–protein interaction, Protein–ligand interaction, Molecular docking, Molecular dynamics, SuFEx-functionalised naphthoquinones

1 PEX5-PEX14 Analysis

1.1 RMSD

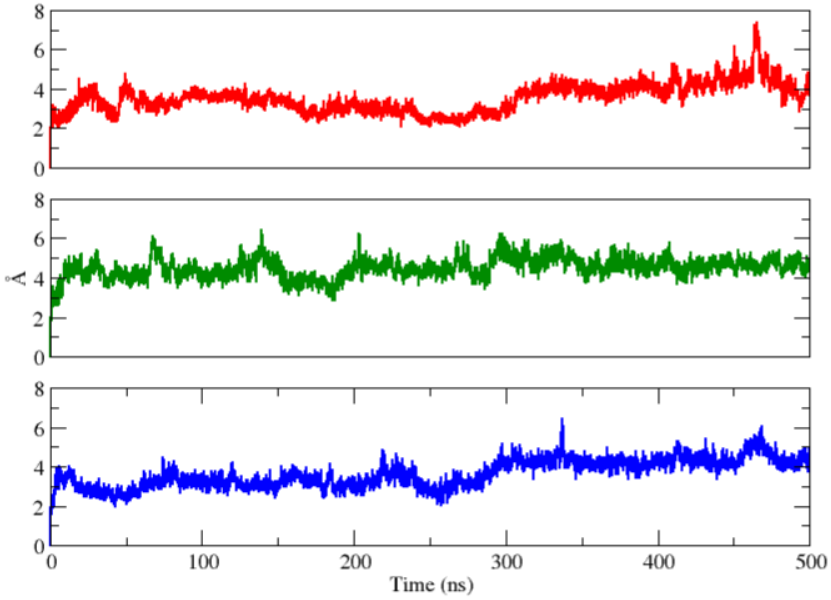

Fig. S1 RMSD of the three simulations of the PEX5-PEX14 protein-protein interaction (PBD code: 8GI0). Run1 (red), Run2 (green) and Run3 (blue).

1.2 Protein-protein Interactions

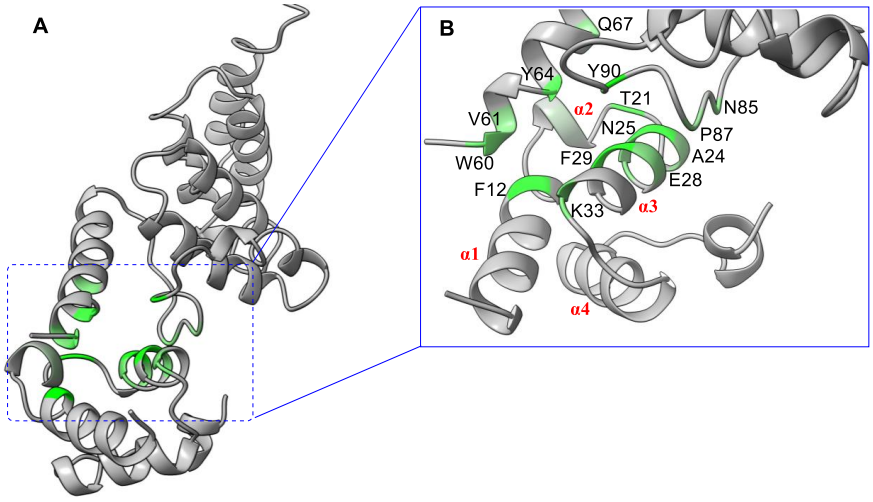

Fig. S2 Amino acid residues involved in PEX5–PEX14 interactions during a 500 ns molecular dynamics simulation.

1.3 Hydrogen Bonds

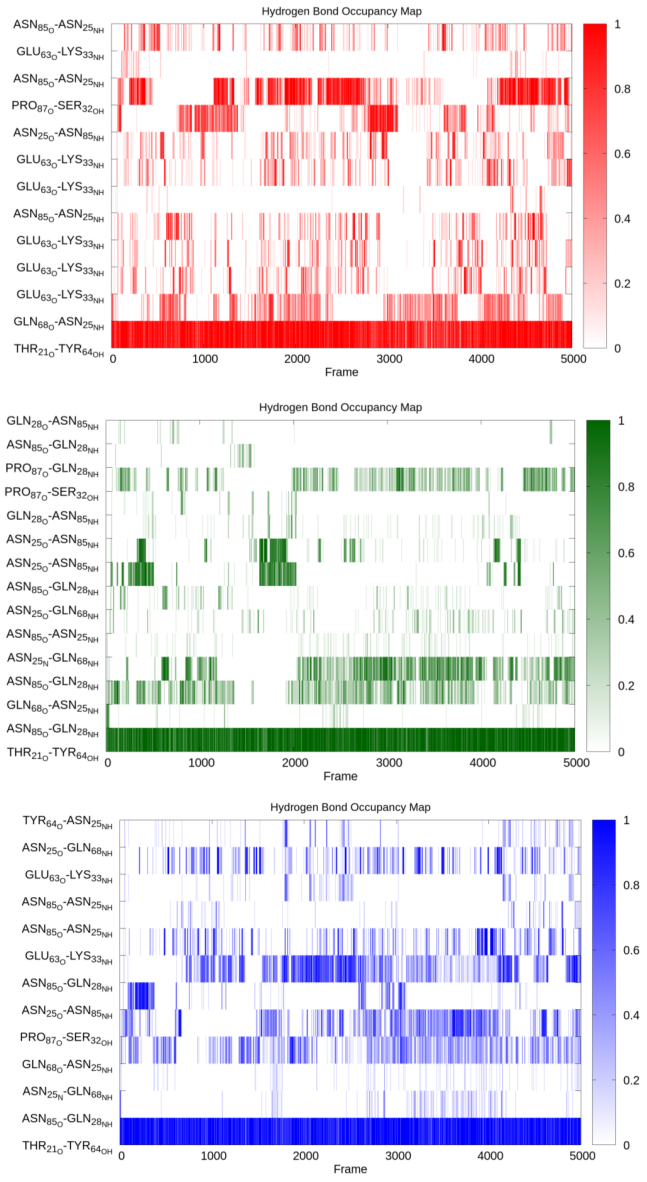

Fig. S3 Time series of selected high-frequency hydrogen bond interactions observed across three independent 500 ns molecular dynamics simulations. Run1 (red), Run2 (green) and Run3 (blue).

2 Ligand-PEX14

2.1 Molecular Docking

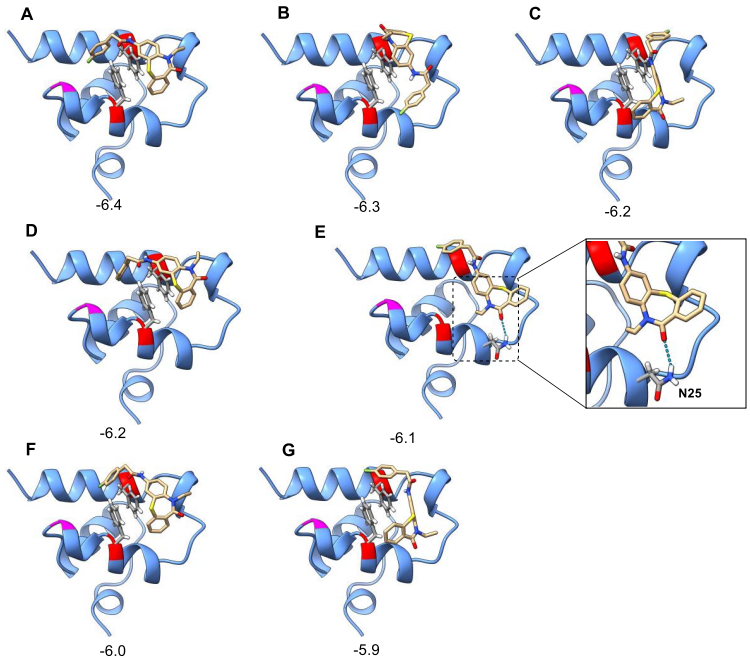

Fig. S4 A-G, Molecular docking poses with corresponding binding scores (kcal mol^{-1}). E, Highlighted hydrogen bond interaction.

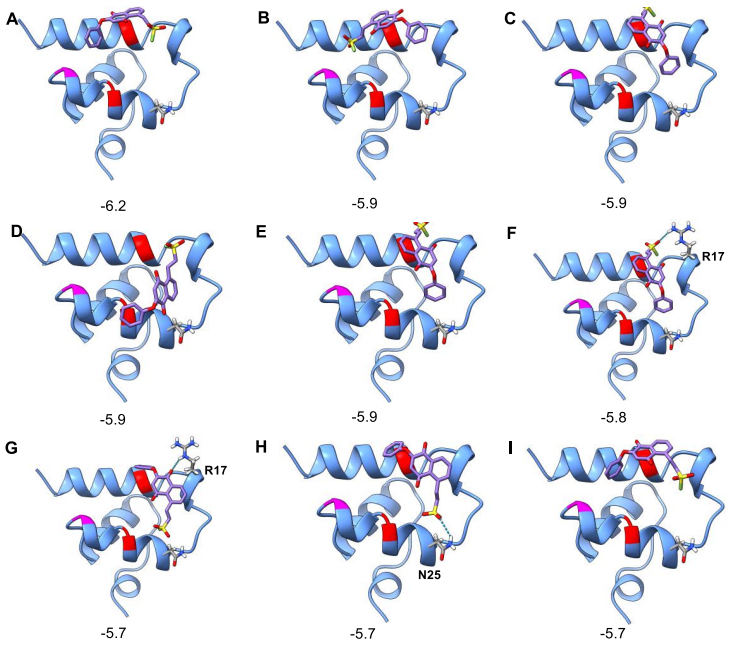

Fig. S5 A–I, Molecular docking poses of the 3L ligand with the corresponding binding scores (kcal mol^{-1}). Dashed blue lines indicate hydrogen-bond interactions.

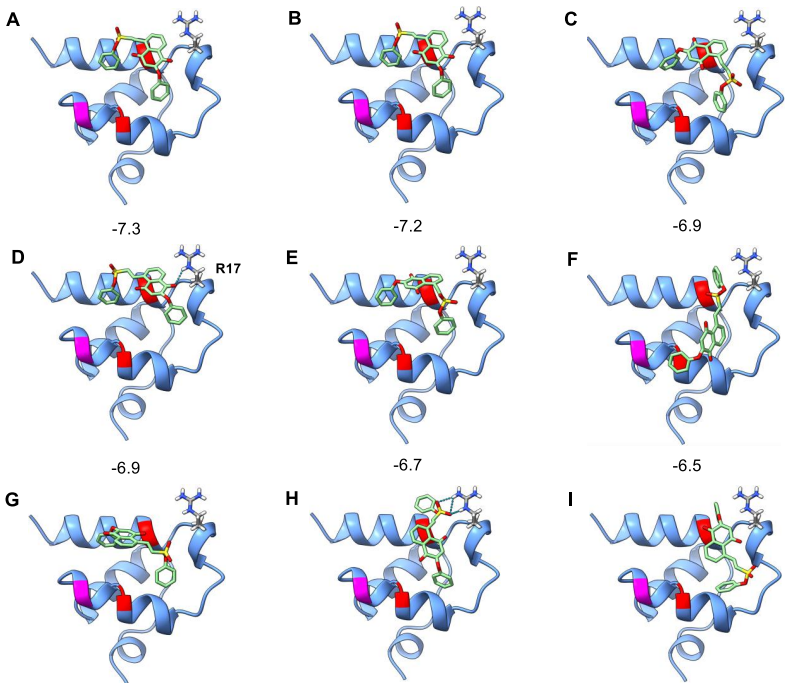

Fig. S6 A–I, Molecular docking poses of the 3L-OAr ligand with the corresponding binding scores (kcal mol^{-1}). Dashed blue lines indicate hydrogen-bond interactions.

2.2 Molecular dynamics analysis of the ligand–PEX14 complex (RMSD)

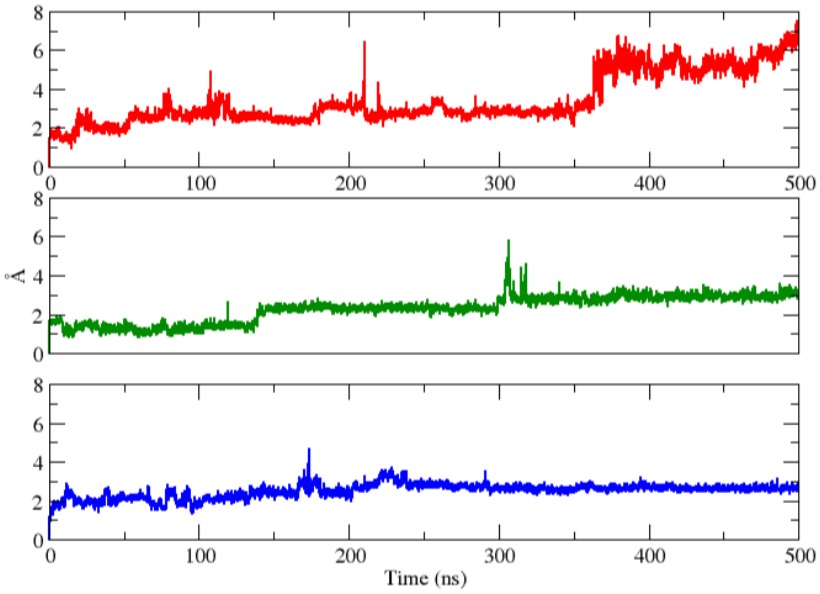

Fig. S7 RMSD of the three simulations of the ET7-PEX14 interaction. Run1 (red), Run2 (green) and Run3 (blue). The increase at ∼360 ns reflects the ligand exiting the PEX14 binding groove and subsequently dissociating from the protein.

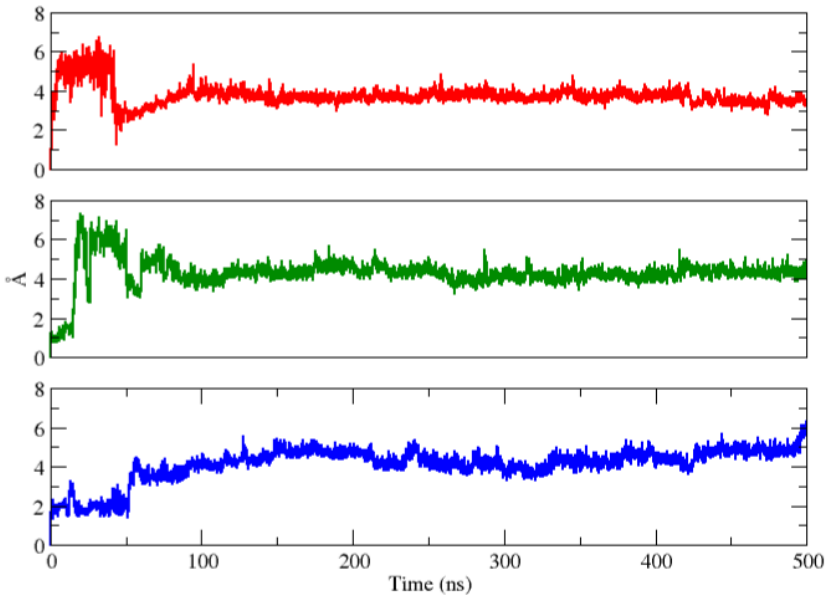

Fig. S8 RMSD of the three simulations of the 3L-PEX14 interaction. Run1 (red), Run2 (green) and Run3 (blue).

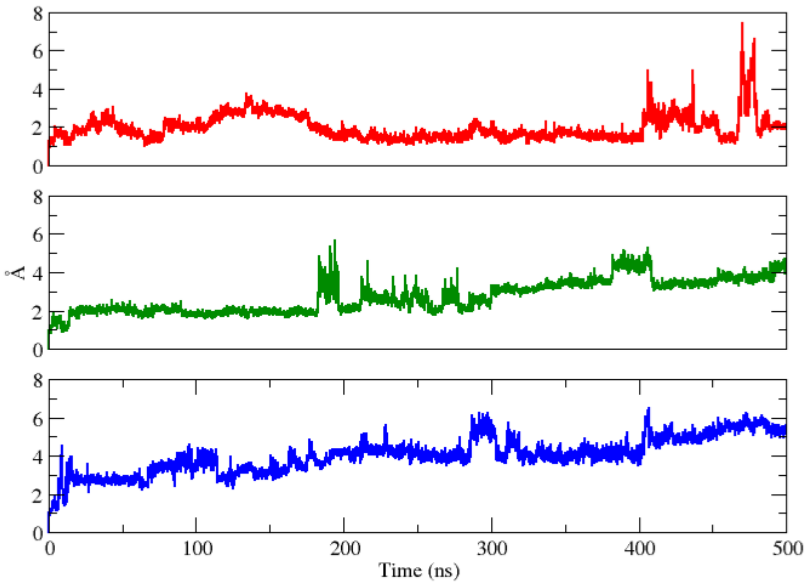

Fig. S9 RMSD of the three simulations of the 3L-OAr-PEX14 interaction. Run1 (red), Run2 (green) and Run3 (blue).

2.3 Ligand Density Distribution on the PEX14 Surface

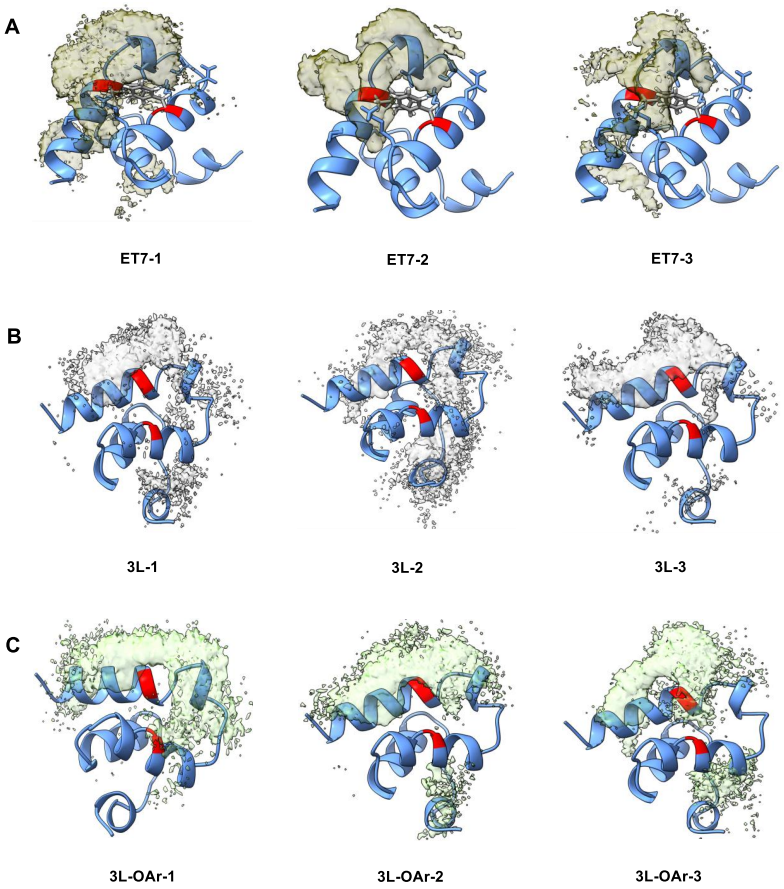

Fig. S10 Ligand trajectories mapped over 500 ns of molecular dynamics simulations: (A) ET7 ligand trajectory, (B) 3L ligand trajectory, and (C) 3L-OAr ligand trajectory.

2.4 Hydrogen Bond Analysis of PEX14 and ET7 inhibitor

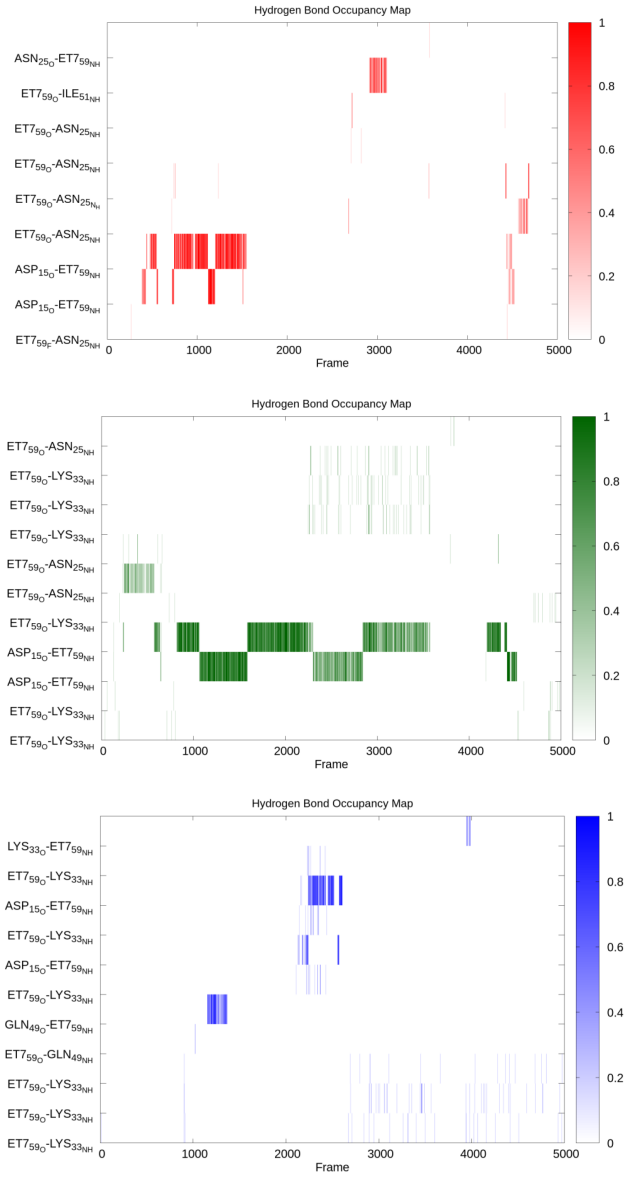

Fig. S11 Time series of selected high-frequency hydrogen bond interactions observed across three independent 500 ns molecular dynamics simulations. Run1 (red), Run2 (green) and Run3 (blue).

2.5 Hydrogen Bond Analysis of PEX14 and 3L inhibitor

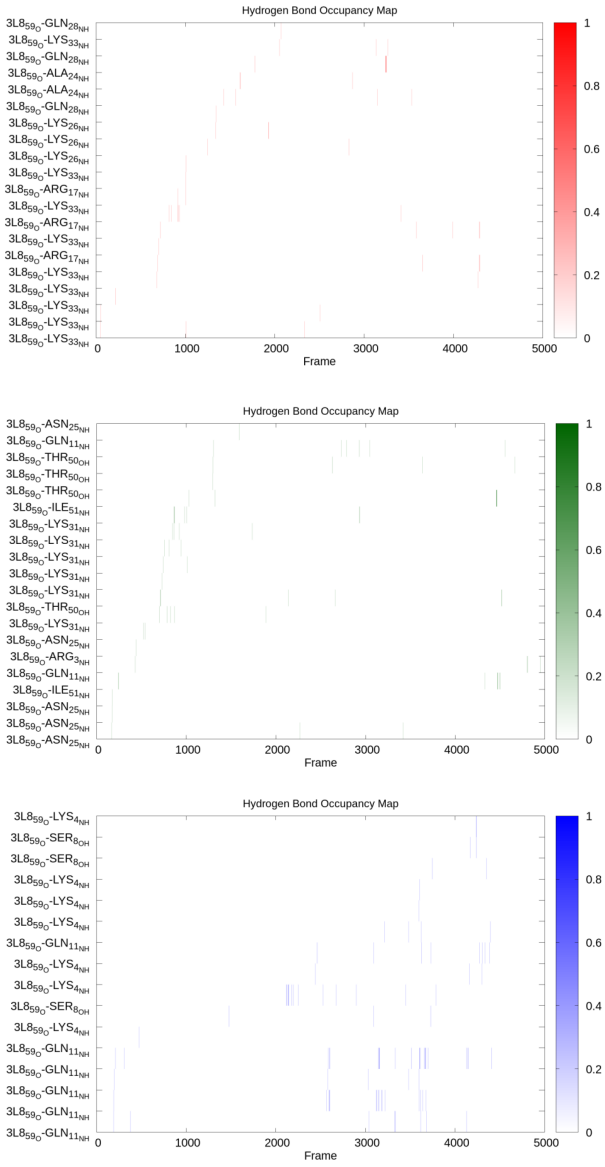

Fig. S12 Time series of selected high-frequency hydrogen bond interactions observed across three independent 500 ns molecular dynamics simulations. Run1 (red), Run2 (green) and Run3 (blue).

2.6 Hydrogen Bond Analysis of PEX14 and 3LARS inhibitor

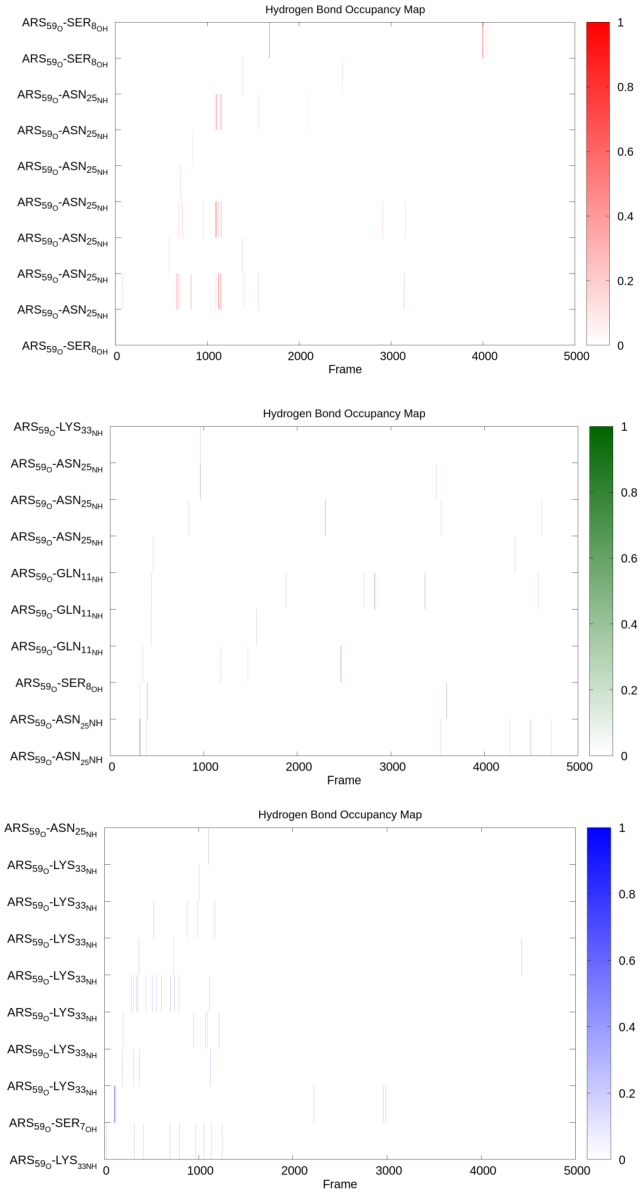

Fig. S13 Time series of selected high-frequency hydrogen bond interactions observed across three independent 500 ns molecular dynamics simulations. Run 1 is shown in red, Run 2 in green, and Run 3 in blue.

2.7 MM-PBSA and percentage of Iterations

The T-shaped π interactions were quantified using geometric criteria based on distance and angular thresholds, defined between ring centers of mass and relative aromatic plane orientations, with interactions considered present when distances were $\leq 5, \text{Å}$ and angles $\leq 90°$.

Table S1 MM-PBSA binding free energy and percentages of T-shaped π and π–cation interactions obtained from three independent 500 ns molecular dynamics simulations of the PEX5–PEX14 complex.

Simulation run	ΔG (kcal mol^{-1})	% T-shape (TYR90$_{\text{face}}$–Phe29$_{\text{edge}}$)	% T-shape (Try64$_{\text{face}}$–Phe12$_{\text{edge}}$)	% π-cation (Trp60-Lys33)
1	-16.71	93.52	99.86	80.96
2	-17.12	96.78	99.72	83.08
3	-15.84	85.92	99.94	86.68

Table S2 MM-PBSA binding free energy and percentages of T-shaped π and π–cation interactions obtained from three independent 500 ns molecular dynamics simulations of the PEX14–ET7 inhibitor complex.

Simulation run	ΔG (kcal mol^{-1})	% T-shape (Phe29$_{\text{face}}$–ET7$_{\text{edge}}$)	% T-shape (ET7$_{\text{face}}$–Phe12$_{\text{edge}}$)	% π-cation (ET7-Lys33)
1	-5.46	23.86	21.16	23.84
2	-6.81	43.64	40.48	16.88
3	-4.09	36.20	34.46	39.22

Table S3 MM-PBSA binding free energy obtained from three independent 500 ns molecular dynamics simulations of the PEX14–3L inhibitor complex.

Simulation run	ΔG (kcal mol^{-1})
1	-3.08
2	0.86
3	-2.07

Table S4 MM-PBSA binding free energy and percentages of T-shaped π and π–cation interactions obtained from three independent 500 ns molecular dynamics simulations of the PEX14–3L-OAr inhibitor complex.

Simulation number	ΔG (kcal mol^{-1})	% T-shape (3L-OAr$_{face}$–Phe12$_{edge}$)	% π-cation (3L-OAr-Lys33)
run 1	-3.23	18.88	1.66
run 2	-5.37	0.74	13.80
run 3	-3.53	17.18	11.00

3 Ligand coordinates

3.1 ET7 inhibitor

Optimized geometry of the ET7 ligand obtained at the ωB97X-D3/def2-SVP level of theory

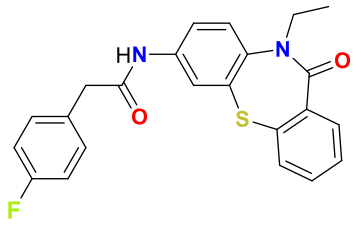

Structure of ET7 ligand.

C	158.47100	109.68400	222.18900
C	159.45000	110.59400	222.93300
N	160.54900	111.05000	222.01200
C	161.75000	110.42900	222.15600
O	161.81900	109.55200	223.01700
C	162.88800	110.68900	221.38300
C	164.07500	110.82200	222.11000
C	162.91000	110.82400	220.00200
C	165.27600	111.08300	221.44000
C	165.29900	111.21900	220.05600
C	164.10900	111.08800	219.33500
S	161.49300	110.70200	218.95300
C	160.58300	111.98000	219.73400
C	160.21600	113.03400	218.87300
C	160.25000	112.00500	221.08500

C	159.47800	114.12800	219.35900
C	159.15400	114.13800	220.72200
C	159.52800	113.10100	221.57200
N	159.07800	115.20600	218.62600
C	158.83200	115.19000	217.28600
O	158.91400	114.22300	216.53500
C	158.40600	116.54100	216.70000
C	159.48200	117.12200	216.01200
C	160.52400	117.71400	216.73200
C	161.59600	118.28900	216.04100
C	161.62200	118.27100	214.64300
F	162.66000	118.82700	213.98600
C	160.58800	117.67600	213.92300
C	159.51500	117.10100	214.61200
H	164.11800	111.19100	218.26000
H	166.23000	111.42400	219.54900
H	166.19600	111.18100	221.99800
H	164.06400	110.72300	223.18500
H	158.91600	111.46200	223.31900
H	159.88300	110.05200	223.77400
H	158.03000	110.22900	221.35400
H	159.00200	108.81000	221.81100
H	158.71000	116.63900	214.06000
H	160.62000	117.66200	212.84400
H	162.40600	118.74800	216.58700
H	160.49700	117.72500	217.81200
H	157.57300	116.39200	216.01300
H	158.09100	117.20300	217.50600
H	158.97200	115.95100	219.04100
H	158.59900	114.98000	221.10900
H	159.25600	113.14800	222.61600
H	160.50200	113.00500	217.83200
H	157.68300	109.36400	222.87000

3.2 3L inhibitor

Optimized geometry of the 3L ligand obtained at the ωB97X-D3/def2-SVP level of theory

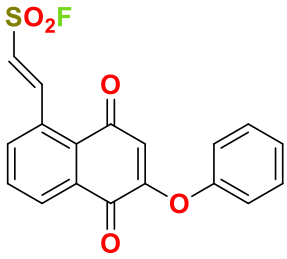

Structure of 3L ligand

C	158.65900	110.39300	214.78400
C	158.77700	111.23700	215.89700
C	159.60400	110.83900	216.96400
C	160.29100	109.61800	216.88700
C	160.15700	108.78900	215.77300
C	159.33600	109.17900	214.72200
C	159.73000	111.68200	218.20100
C	161.19800	109.16200	217.98700
C	160.66600	111.24400	219.24800
C	161.34500	110.08200	219.16900
O	161.79300	108.11500	217.94200
O	159.07600	112.69600	218.34100
C	158.04700	112.52500	215.89000
C	158.38900	113.53800	215.09000
S	157.58500	115.08200	215.24300
F	158.88000	116.03300	215.21700
O	157.04400	115.20700	216.56900
O	156.82900	115.39700	214.06200
O	162.19600	109.59900	220.07400
C	163.22200	110.40800	220.53300
C	163.30000	110.69600	221.89200
C	164.31200	111.54100	222.34500
C	165.22900	112.08400	221.44600
C	165.13200	111.78700	220.08700
C	164.12400	110.94500	219.62100
H	158.03000	110.69100	213.95800
H	160.68800	107.85000	215.72800
H	159.22400	108.54100	213.85800
H	160.81500	111.87600	220.11100
H	157.20700	112.65000	216.55700
H	159.16200	113.40300	214.34800
H	162.58800	110.27200	222.58500
H	164.38600	111.77600	223.39700

H	166.01400	112.73400	221.80200
H	165.84100	112.21200	219.39200
H	164.04500	110.71300	218.56900

3.3 3L-OAr inhibitor

Optimized geometry of the 3L-OAr ligand obtained at the ωB97X-D3/def2-SVP level of theory

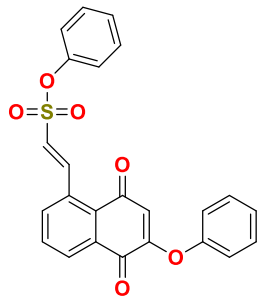

Structure of 3L-OAr ligand

C	158.70700	112.68900	216.77200
C	158.69100	111.30200	217.00300
C	158.21400	113.19700	215.56000
C	157.69000	112.34300	214.58900
C	157.66000	110.97300	214.82200
C	158.16100	110.46000	216.01600
C	158.23700	114.66200	215.26600
C	159.19800	113.63600	217.82600
C	159.28000	115.06500	217.49500
C	158.83000	115.55700	216.32300
O	157.81600	115.12400	214.23500
O	159.51100	113.23800	218.93300
C	159.23800	110.69300	218.23800
C	160.14000	109.71200	218.21600
S	160.80500	109.09800	219.72800
O	162.04200	108.39900	219.49000
O	159.71500	108.50600	220.47200
O	161.28100	110.46700	220.48600
C	162.63000	110.78700	220.52200
C	163.33300	110.51100	221.69200
C	164.68000	110.85900	221.76500
C	165.31100	111.46400	220.67800
C	164.59100	111.72800	219.51200
C	163.24100	111.39200	219.42600

O	158.84000	116.83500	215.94500
C	160.03000	117.40000	215.51600
C	160.33700	117.37200	214.16000
C	161.51500	117.97400	213.72200
C	162.36800	118.59400	214.63600
C	162.04100	118.61600	215.99100
C	160.86500	118.01800	216.44100
H	159.71200	115.75900	218.20100
H	160.59800	118.02900	217.48700
H	163.28200	119.05700	214.29300
H	162.70000	119.09800	216.69800
H	159.66700	116.88900	213.46400
H	161.77000	117.96200	212.67300
H	157.31000	112.74700	213.66200
H	157.24800	110.30800	214.07800
H	158.13600	109.39200	216.17400
H	158.90700	111.04200	219.20500
H	160.46200	109.29500	217.27300
H	162.83300	110.03500	222.52300
H	165.08600	112.19500	218.67300
H	162.67000	111.59200	218.53200
H	165.24100	110.66100	222.66600
H	166.35600	111.72800	220.73900